Coastal Engineering 57 (2010) 317–330

Contents lists available at ScienceDirect

Coastal Engineering

journal homepage: www.elsevier.com/locate/coastaleng

Numerical modelling of short- and long-wave transformation on a barred beach

Alec Torres-Freyermuth *, Javier L. Lara, Inigo J. Losada

Environmental Hydraulics Institute, "IH Cantabria", Universidad de Cantabria, Avda. de los Castros s/n, Santander 39005, Spain

ARTICLE INFO

Article history:
Received 6 June 2008
Received in revised form 21 October 2009
Accepted 26 October 2009

Keywords:
Nearshore
Surf zone
Long-waves
Low-frequency waves
RANS

ABSTRACT

This work aims to demonstrate an advancement towards the integrated modelling of surf zone hydrodynamics by means of a VOF-type numerical model (COBRAS-UC) based on the Reynolds-Averaged Navier–Stokes equations. In this paper, the numerical model is adapted and validated for the study of nearshore processes on a mildly-sloping beach. The model prediction of wave energy transformation and higher order statistics (skewness and asymmetry) are in good agreement with detailed laboratory observations from a barred beach [Boers, M. (1996). "Simulation of a surf zone with a barred beach; Report 1: Wave heights and wave breaking". Tech. Rep.96-5, Comm. on Hydrol. and Geol. Eng., Dept. of Civil Engineering, Delft University of Technology]. Moreover, the numerical model allows us to study the low-frequency motions inside the surf zone. It is found that in order to achieve a satisfactory simulation of both short- and long-wave transformation, the numerical model must achieve: (i) the simultaneous second-order wave generation and absorption, (ii) the energy transfer between triad of components, (iii) the short- and long-wave energy dissipation inside the surf zone, and (iv) the wave reflection at the shoreline. Comparisons between numerical and experimental results demonstrate the model capability to satisfactorily simulate all the aforementioned processes.

1. Introduction

The modelling of nearshore hydrodynamics requires an accurate reproduction of the complex interaction between small- and large-scale motions throughout the water column in order to understand more complex features such as sediment transport. Field and laboratory measurements have demonstrated that low-frequency motions represent an important contribution to the total energy budget inside the surf zone. These motions are also referred to as long-waves, infragravity waves, subharmonic gravity waves, or 'surf beat', being the latter the term employed by Munk (1949) to describe this phenomenon for the first time. The relevance of their study relies on the fact that sediment transport (Holman and Bowen, 1982; Aagaard and Greenwood, 2008), harbor resonance (Sand, 1982), the modification of the incident short-wave field (Goda, 1975), and coastal inundation (Péquignet et al., 2009) are directly or indirectly related to motions which occur in the low-frequency band of the spectrum. Therefore, an accurate representation of these motions must be considered in every nearshore wave propagation model.

The numerical study of nonlinear shallow water wave dynamics has traditionally been approached using either Nonlinear Shallow Water (NSW) or Boussinesq-type equations models. Both theories give satisfactory results if the underlying assumptions are not violated. A nonlinear approach, including the feedback between short- (high-frequency) and long- (low-frequency) waves was achieved using a NSW equation model in Watson and Peregrine (1992). The capability of one-dimensional depth-averaged NSW equations models for the study of the surf zone (e.g. Raubenheimer et al., 1996; Elgar et al., 1997; Raubenheimer, 2002) and swash zone (e.g. Kobayashi and Wurjanto, 1992; Raubenheimer et al., 1995; Raubenheimer and Guza, 1996) hydrodynamics has been successfully tested on natural beaches, finding qualitatively good agreement between observations and model predictions. Unfortunately, NSW equations models are not able to resolve the vertical velocity structure. Moreover, the energy transfer to higher frequencies occurring outside the surf zone cannot be resolved accurately due to the lack of dispersion in this type of models. These limitations seems to be overcome with the recent advent of two-layer nonlinear models (e.g. Lynett and Liu, 2004; Zijlema and Stelling, 2008).

Boussinesq-type of models are able to include frequency dispersion, a depth-dependent velocity profile, and can be applied to both breaking and non-breaking waves. A great effort has been devoted in order to relax the original equations by deriving the extended Boussinesq equations (Kirby, 2003). However, inside the surf zone, this type of models requires setting both the triggering wave breaking mechanism (e.g. Schaffer et al., 1993; Kennedy et al., 2000; D'Alessandro and Tomasichio, 2008) and the subsequent wave energy dissipation due to wave breaking (e.g. Mase and Kirby, 1992; Kaihatu and Kirby, 1995). Regarding the latter, wave breaking formulations have been

---

* Corresponding author. Now at Instituto de Ingeniería, Laboratorio de Ingeniería y Procesos Costeros, Universidad Nacional Autónoma de México, Puerto de Abrigo s/n, Sisal, Yucatán 97355, México. Tel.: +34 942 201810; fax: +34 942 201860.
E-mail address: atorresf@ii.unam.mx (A. Torres-Freyermuth).

0378-3839/$ – see front matter © 2009 Elsevier B.V. All rights reserved.
doi:10.1016/j.coastaleng.2009.10.013

implemented based on a detailed calculation of generation and transport of vorticity and turbulent kinetic energy (e.g. Veeramony and Svendsen, 2000), the surface roller dissipation (e.g. Madsen et al., 1997), or an eddy-viscosity breaking type model, which requires setting the coefficient for the wave breaking scheme empirically. Despite these limitations, numerical models based on Boussinesq equations have been successfully employed to simulate wave transformation in the nearshore (e.g. Bayram and Larson, 2000; Chen et al., 2003; Lynett, 2006a,b) and low-frequency motions observed in the laboratory (e.g. Madsen et al., 1997; Karunarathna et al., 2005). However, these models failed to reproducethe strong nonlinear shoaling prior to wave breaking, and the free-surface higher order statistics (i.e. skewness and kurtosis) which are thought to be relevant for sediment transport studies (Hoefel and Elgar, 2003; Hsu and Hanes, 2004).

Thus, the general need to describe wave transformation inside the surf zone has focused our attention on the application of Navier–Stokes solvers. In theory, any incompressible Newtonian fluid can be described by the conservation of mass and momentum Navier–Stokes equations. However, a direct solution of these equations for the study of breaking waves for practical purposes is not yet possible, due to the extremely large computational effort which is required to resolve the smallest scale of turbulence for large Reynolds number flows under breaking waves. This limitation can be overcome by the use of a statistical approximation to the turbulence closure problem in the Reynolds-Averaged Navier–Stokes (RANS) formulation.

Numerical models based on the RANS equations have been successfully applied in various coastal engineering applications. The study of wave-structure interaction (e.g. Hsu et al., 2002; Garcia et al., 2004; Losada et al., 2005; Lara et al., 2006a), surf zone (e.g. Lin and Liu, 1998a,b; Lara et al., 2006b) and swash zone (e.g. Puleo et al., 2007) hydrodynamics, and sediment transport (e.g. Hsu and Liu, 2004) have been satisfactorily simulated with COrnell BReaking waves And Structures (Lin and Liu, 1998a,b). However, most of these studies have focused on the model validation and the study of processes at the time scale of short-waves.

The original COBRAS code has been improved upon in later studies, increasing the model's robustness and stability and reducing the computational cost by rewriting an important part of the code, with the aim of making it useful for different applications. The improvements cover the wave generation process; code updating and refactoring; optimization and improvement of the main subroutines; improvement of input and output data definition; the development of a graphical user interface and a set of post-processing tools. These modifications included in COBRAS-UC (Losada et al., 2008) have been thoroughly tested and validated for wave-structure interaction (e.g. Lara et al., 2008; Losada et al., 2008; Guanche et al., 2009) and wave breaking (e.g. Torres-Freyermuth et al., 2007). The improvement of model robustness and stability allows approaching problems at prototype scale and/or consider $O(10^2)$ of waves. More recently, surf zone hydrodynamics on natural beaches have been satisfactorily simulated using RANS models (e.g. Torres-Freyermuth et al., 2007; Chopakatla et al., 2008). Free-surface elevation, bottom pressure, and wave-induced velocity, corresponding to the SwashX field experiment (Raubenheimer, 2002), were satisfactorily simulated using COBRAS-UC in Torres-Freyermuth et al. (2007). However, the capability to carry out an analysis of the differences between observations and model predictions, and the detailed study of infragravity motions was constraint by the many uncertainties present in a natural environment and three-dimensional effects not accounted for by the numerical model. Hence the model requires a more rigorous validation of its capability for simulating the short- and long-wave interaction.

In summary, the modelling of short- and long-wave transformations inside the surf zone is a complex problem. The breaking process needs to be parameterized in most of the existing surf zone hydrodynamic models, and hence the numerical results reported in the literature often represent a best fit of the models parameters to the measured data. These parameters are site/case-dependent and hence their universal application is still not possible. Moreover, the existing wave breaking parameterizations have problems to achieve simultaneously a good description of both the energy dissipation and the higher order statistics of the spectrum (i.e. skewness and asymmetry). In this paper, we investigate in which extent the use of a RANS model can improve the current limitations in the modelling of short- and long- wave transformation (and their interactions) inside the surf zone. This paper is organized as follows. The laboratory experiments by Boers (1996) are briefly described in Section 2. In Section 3, the numerical model is described emphasizing the new wave generation procedure implemented as part of this work. The numerical setup of the simulated tests is also described in this section. The model validation is presented in Section 4, followed by a detailed study of low-frequency motions (Section 5). Finally, the concluding remarks and future work are outlined in Section 6.

2. Experimental setup (Boers, 1996)

The laboratory experiments were carried out by Boers (1996) in the Large Wave Flume of the Fluid Mechanics Laboratory at Delft University of Technology. The flume is 40 m-long, 0.80 m-wide and 1.5 m-high. The experiments are the Froude scale reproduction of the LIP 11D-experiments (Roelvink and Reniers, 1995). The still water level during the experiments was set at 0.75 m with respect to the bottom at the wave paddle position. The used smoothed fixed bathymetry resembles a mild-slope barred beach profile. The wave gauge closest to the wave board is located at the toe of the beach profile at $x=0$ m (Fig. 1). A flat bottom part extends from the toe to $x=-5$ m where the wave board is located. Three different target wave conditions were generated during the experiments (see Table 1) using repeated (7–11 cycles) series of about a hundred irregular waves. The flume is equipped with a piston-type wave board with second-order control, and a wave absorption system that minimizes re-reflections at the wave board from the shore-reflected wave energy. Free-surface elevation time series from 70 cross-shore locations sampled at 20 Hz, provide high spatial and temporal resolution data for the analysis of short- and long-wave transformation. The sensors are identified in this study with the acronym 'WG' followed by the gauge number (i.e. WG1, WG2,...,WG70). However, due to restrictions by the limited excursion of the wave board the measured signals are high-pass filtered at $f_p/5$ for Test 1B and at $f_p/10$ for Tests 1A and 1C following a previous study by Janssen et al. (2003). Furthermore, Boers (1996) recorded video at different cross-shore position along the flume in order to detect the presence of rollers on the wave front during the experiments, reporting the presence of breaking waves (rollers) in the entire wave flume in Tests 1A and 1B. However, in Test 1A the fraction of roller is less in the foreshore. For further details on the experimental set-up and additional measurements interested readers are referred to Boers (1996, 2005).

3. Numerical model

3.1. Mathematical formulation

The numerical model COBRAS-UC (Losada et al., 2008) is a depth- and phase-resolving wave propagation model based on the Reynolds-Averaged Navier–Stokes (RANS) equations, where the instantaneous velocity, u, and pressure, p, fields are decomposed into mean, $\langle\cdot\rangle$, and turbulent components,

$$\frac{\partial\langle u_i\rangle}{\partial x_i}=0 \tag{1}$$

$$\frac{\partial\langle u_i\rangle}{\partial t}+\langle u_j\rangle\frac{\partial\langle u_i\rangle}{\partial x_j}=-\frac{1}{\rho}\frac{\partial\langle p\rangle}{\partial x_i}+g_i+\frac{1}{\rho}\frac{\partial\langle\tau_{ij}\rangle}{\partial x_j}-\frac{\partial\langle u_i^{\prime}u_j^{\prime}\rangle}{\partial x_j} \tag{2}$$

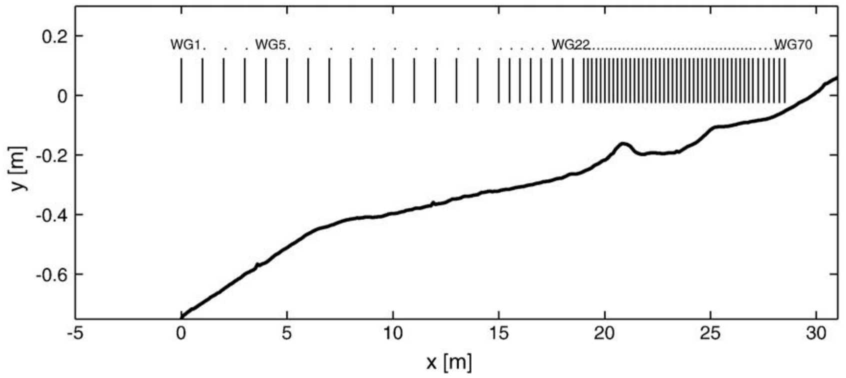

Fig. 1. Experimental setup and wave gauge locations in Boers (1996).

and the $k-\varepsilon$ equations for the turbulent kinetic energy, k, and the turbulent dissipation rate, ε, are given by

$$\frac{\partial k}{\partial t} + \langle u_j\rangle \frac{\partial k}{\partial x_j} = \frac{\partial}{\partial x_j}\left[\left(\frac{\nu_t}{\sigma_k}+\nu\right)\frac{\partial k}{\partial x_j}\right] - \langle u_i' u_j'\rangle \frac{\partial \langle u_i\rangle}{\partial x_j} - \varepsilon \tag{3}$$

$$\begin{aligned}\frac{\partial \varepsilon}{\partial t} + \langle u_j\rangle \frac{\partial \varepsilon}{\partial x_j} = {} & \frac{\partial}{\partial x_j}\left[\left(\frac{\nu_t}{\sigma_\varepsilon}+\nu\right)\frac{\partial \varepsilon}{\partial x_j}\right] \\ & -C_{1\varepsilon}\frac{\varepsilon}{k}\nu_t\left(\frac{\partial \langle u_i\rangle}{\partial x_j}+\frac{\partial \langle u_j\rangle}{\partial x_i}\right)\frac{\partial \langle u_i\rangle}{\partial x_j} \\ & -C_{2\varepsilon}\frac{\varepsilon^2}{k}\end{aligned} \tag{4}$$

where $i, j = 1, 2$ for a two-dimensional flow, ρ is the fluid density, g_i is the ith component of the gravitational acceleration, $\langle \tau_{ij}\rangle$ is the viscous stress tensor of the mean flow, and ν_t is the eddy viscosity. For a Newtonian fluid, $\langle \tau_{ij}\rangle = 2\mu\langle \sigma_{ij}\rangle$ with μ being the molecular viscosity and $\langle \sigma_{ij}\rangle = 1/2(\partial\langle u_i\rangle/\partial x_j + \partial\langle u_j\rangle/\partial x_i)$, the mean rate of strain. The influence of turbulence fluctuations on the mean flow field is represented by the Reynolds stresses $\rho\langle u_i' u_j'\rangle$. The governing equationsfor k and ε are derived from the Navier–Stokes equations and higher order correlations of turbulence fluctuations in k and ε equations are replaced by closure conditions. The empirical coefficients in Eq. (4) ($C_{1\varepsilon} = 1.44$, $C_{2\varepsilon} = 1.92$, $\sigma_\varepsilon = 1.3$, and $\sigma_k = 1.0$) were experimentally determined from stationary flows (Rodi, 1980). A nonlinear algebraic Reynolds stress model is used to relate the Reynolds stress tensor and the strain rate of mean flow (Rodi, 1980; Lin and Liu, 1998a).

The RANS equations are solved by the finite difference two-step projection method (Chorin, 1968, 1969). In order to track free-surface locations, the volume of fluid (VOF) method is used (Hirt and Nichols, 1990). For more details, interested readers are referred to the papers of Lin and Liu (1998a,b) where model equations, coefficient values, and boundary and initial conditions of the original code named COBRAS were first introduced.

3.2. Forcing boundary condition

The study of nearshore hydrodynamics on beaches must consider the contribution from the subharmonic frequencies in the incident wave spectra, since they represent an important fraction of the total energy budget close to shore. The incident bound waves are found to have significant amplitude growth in mildly-sloping beaches (Battjes et al., 2004). Therefore, the model application on a mild-slope beach regime requires an improvement of the existing wave generation procedures in COBRAS-UC in order to reproduce the high-frequency (hf hereinafter) and low frequency (lf hereinafter) motions accurately. The incident (second-order) spectrum is calculated from the high-passed measured signal (e.g. $0.5f_p<f$), at the seawardmost sensor (i.e. WG1), following Longuet-Higgins and Stewart (1960) (see also Baldock et al., 1996). The input free-surface elevation time series is defined as the linear superposition between primary-frequency waves (high-pass filtered of the original signal) and the bound-long wave (second-order contribution), whereas the corresponding velocity profile in the latter is calculated trough the second-order velocity potential (see Appendix A for details).

Table 1
Wave characteristics simulated by Boers (1996).

Test	H_s [m]	T_P [s]	Cycle period [s]
1A	0.16	2.05	157.079
1B	0.21	2.03	157.079
1C	0.10	3.33	245.441

The measured surface elevation density spectrum and the second-order solution used to drive the numerical model, for one of the simulated tests (Test 1C), are shown in Fig. 2. The additional energy measured in the lf-band ($f<0.5f_p$), with respect to the second-order estimation, corresponds to the reflected free lf-wave energy reaching this location. This energy is expected to be matched at the end of the model simulation and must be canceled out by the active absorption system in order to avoid re-reflection. Therefore, another goal is to achieve the long-wave absorption of the reflected free-wave reaching the inflow boundary. The active wave absorption term refers to the use of a wavemaker as a moving boundary which cancels out the incoming wave by generating a wave of equal amplitude and opposite phase (Troch and Rouck, 1999). The reflected wave reaching the generating boundary is detected as the free-surface difference, η', between the target and the observed free-surface elevation signal at each time step. For the mildly-sloping beach case, where most of the hf-wave energy is dissipated in the surf zone, the reflected wave may be approximated as a non-dispersive long-wave with an amplitude η' and uniform horizontal velocity $u' = \eta'\sqrt{g(h+\eta')}$. Linear superposition of incident and reflected wave components at the boundary assumes that nonlinear effects are negligible. This latter assumption is widely employed for wave generation and absorption in nearshore wave propagation models (e.g. Kobayashi et al., 1987; van Dongeren and Svendsen, 1997).

The simultaneous wave generation and (long-wave) absorption is tested using the random wave conditions from Test 1C (Table 1). The simulated time is 245 s, which corresponds to approximately 100 waves. In order to evaluate the improvement of wave forcing due to the wave absorption condition, the wave generation procedure is first tested with the long-wave absorption turned off. The wave generation is satisfactory during the first 40 s, which is the time that it takes for the leading lf-wave to travel from the generation boundary to the shore and back to the generation boundary again as a free-wave. In this case, the lf-waves become trapped inside the computational

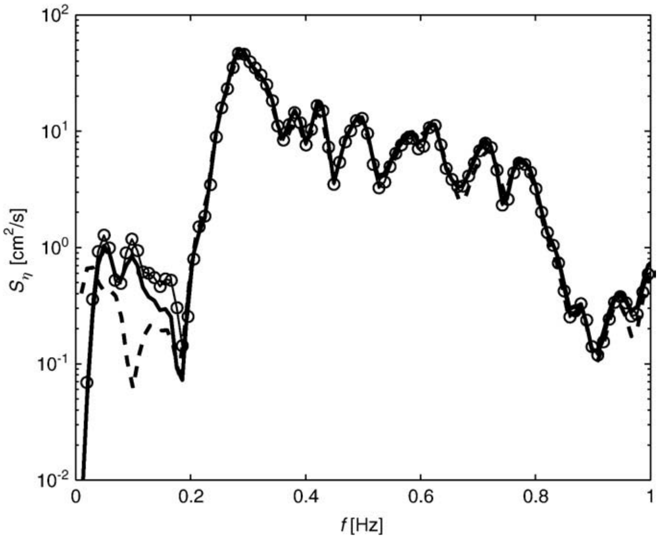

Fig. 2. Total measured energy spectra, at WG1, in the laboratory (open circles), in the numerical model boundary (solid line), and the second-order solution (dashed line) employed to initialized the model in Test 1C.

domain, producing an increase in the water level owing to the mass transport introduced in the numerical wave flume. As a consequence, the wave generation is degraded (not shown). The relative mass variation shows a sustained increment causing a water level increase inside the computational domain (dark line, Fig. 3). On the other hand, when the wave-absorption boundary condition is turned on, a significant improvement in the wave generation at the boundary is achieved for the complete run. The mass presents the expected fluctuations due to the short-wave induced mass transport (Fig. 3, light line) but it does not show an accumulation inside the computational domain as do the previous test. The overall balance gives a close to zero net mass change at the end of the simulation, as it would be expected in a laboratory wave flume. The surface elevation density spectrum at the generating boundary (solid line, Fig. 2) is satisfactory for all frequencies ($0.03<f<1.0$ Hz).

The model sensitivity to wave generation description at the generating boundary is also tested by feeding the model with either the (total) measured signal at WG1 or using only the primary frequencies (band-passed filtered) signal. In both cases (not shown) the hf-energy components are in good agreement with observations. However, significant differences at lower frequencies are observed, highlighting the importance of including second-order wave generation when the study of lf-wave transformation is sought.

3.2.1. Numerical implementation of the simulated tests

The computational mesh employed for the simulated tests is 32 m long and 1 m high. The computational domain does not include the flat bottom section of the wave tank ($x=-5$ to $x=0$ m in Fig. 1) from which no free-surface elevation measurements are available. The grid system employed is nonuniform in the horizontal, x, and vertical, y, directions. Two different meshes were tested: a coarse mesh presenting a minimum cell size with $\Delta x=4$ cm and $\Delta y=2$ cm within the surf zone, resulting in a computational domain of 552×51 cells; and a finer mesh in which the total number of cells is 2202×82, with a minimum cell size of $\Delta x=1$ cm and $\Delta y=1$ cm. In this paper, only the finer mesh results will be presented and discussed.

The wave generation procedure described in Appendix A is applied to the measured time series at WG1 in order to derive the input signal. No further assumption is required, since the laboratory experiments involve normally incident waves over an impermeable beach profile with straight and parallel contours. Therefore, three dimensional effects, which are not accounted for by the numerical model, are expected to be small. The simulated tests corresponds to the steep-(Tests 1A and 1B) and mild-(Test 1C) slope waves of Boers (1996). These runs consisted of 158-s and 245-s periods (~100 waves) (see Table 1), respectively.

The numerical model provides the mean flow characteristics through the solution of Eqs. (1) and (2). Thus, it must be compared against the ensemble average of the realizations (cycles) obtained in the laboratory (see Table 1). The model frequency output was set equal to 20 Hz, to be consistent with the laboratory data sampling rate. The time step, with an order of magnitude of $O(10^{-5})$s), is automatically adjusted during the computation to satisfy the stability constraint (Lin and Liu, 1998a). The CPU-time for the 158-s and 245-s simulations are of 24 and 46 h on a 3.2 GHz desktop PC for Test 1A/1B and Test 1C, respectively.

4. Model validation

The numerical model is validated against the (high-resolution) laboratory observations of Boers (1996). Specifically, free-surface elevation time series, energy density spectra, hf- and lf-significant wave heights, and higher order statistics are compared with the (ensemble averaged) observations. Differences between observations and model predictions are discussed. The same data have been simulated in previous studies (e.g. Zijlema and Stelling, 2008; Janssen, 2006). However, these studies were not able to reproduce the lf-wave transformation inside the surf. This limitation was ascribed to the re-reflection from the generation boundary in the numerical model (e.g. Zijlema and Stelling, 2008) and the wave breaking parameterization (e.g. Janssen, 2006). These two limitations are overcome in the present investigation by means of the implementation of a new boundary condition (Section 2) and relaying on the k–ε turbulence model, with standard coefficients (Rodi, 1980), for simulating the breaking wave process.

4.1. Energy transformation

The free-surface elevation time series from the seawardmost sensor (WG1) is used to feed the numerical model. In this way, the predicted free-surface elevation time series can be directly compared

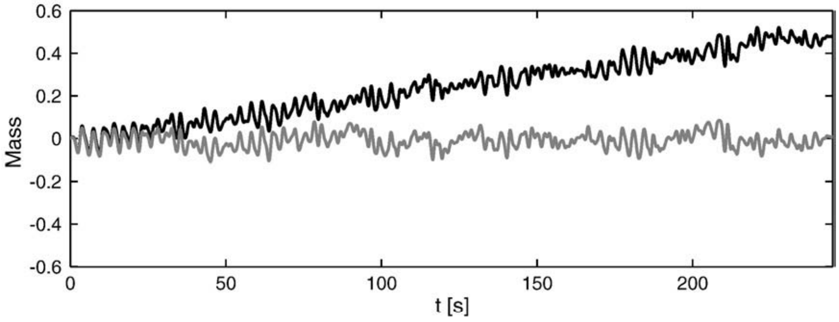

Fig. 3. Relative mass variation along the simulation for Test 1C with active wave absorption (light line) and without active wave absorption (dark line).

with laboratory measurements. Fig. 4 shows the measured (solid line) and predicted (dashed line) free-surface elevation time series at different cross-shore positions in Test 1C. The selected sensors represent different flow regimes across the nearshore. Sensors are located in the numerical model's generation boundary (WG1), shoaling zone (WG10), onset of wave breaking (WG25), wave breaking (WG30), outer surf zone (WG55), and inner surf zone (WG65). A wave amplitude increase is observed from WG1 to WG30 due to shoaling. The free-surface elevation shape becomes more peaked and asymmetric as it approaches breaking. Inside the surf zone (i.e. WG55 and WG65), the model resembles the saw-tooth shape characteristic of broken waves. Small differences in phase and magnitude between model and observations can be ascribed to the earlier breaking in the model. Despite these differences, the model is able to satisfactorily capture the magnitude and phase of most waves in the incident wave train.

With the aim of investigating the energy transformation across the nearshore, the free-surface density spectra at different cross-shore locations are compared with the one observed at the seawardmost sensor (Figs. 5 and 6). For the steep-slope wave case (Test 1A), the sensor located at $x=17$ m (Fig. 5a) presents a hf-energy decrease with respect to the offshore observation (dashed line) due to short-wave breaking. On the other hand, the lf-energy band ($f<0.5f_p$ Hz) is increased owing to shoaling and energy transfer from higher frequencies. A significant hf-energy drop occurs onshore the outer bar (Fig. 5c–d) where most of the waves break. The hf-energy is almost completely dissipated at the inner surf zone (Fig. 5d) whereas the lf-energy ($0<f<0.5f_p$) becomes predominant.

Contrary to the steep-slope test, in Test 1C there is a small energy increase in the hf-band ($0.5f_p<f$ Hz) at $x=17$ m (Fig. 6a) due to short-wave shoaling, whereas the lf-energy does not present a significant increase with respect to the offshore location. The density spectra at the outer breaking bar (Fig. 6b) shows an increase in both, hf- and lf-energy. The shorewardmost sensors (Fig. 6c–d) present energy dissipation in the hf-energy and maximum values of the lf-motions due to the shoreline reflection. An overall good agreement is observed at all sensor locations for both tests. The larger differences are observed for the higher frequencies in the shorewardmost sensors.

In order to gain more insight into the numerical model capability to capture the energy transformation across the nearshore, the hf- ($0.5f_p<f$ Hz) and lf- ($f<0.5f_p$ Hz) significant wave height H_s, here defined as four times the standard deviation of the time series, as a function of cross-shore position are computed using both laboratory and numerical data from the three cases (Fig. 7). The model is able to capture the sustained hf-wave height decrease (increase) from $x=0$ m to $x=20$ m in Test 1A/1B (Test 1C). As previously discussed in Lin and Liu (1998a), the turbulence closure model overestimates the turbulence level near the breaking point producing earlier breaking. This model's inaccuracy to predict the exact breakingpoint location produces a small mass and momentum flux deficit inside the surf zone. This issue is more evident in the more energetic case (Test 1B). The effect of the energy and momentum deficit across the surf zone becomes evident in Fig. 8, where model predictions lay below the line of perfect agreement for small values of H_s. However, the H_s predicted is very satisfactory with a relative mean error of 4.41% and a correlation of $r^2=0.99$ considering all data points (210 points). It is important to point out the challenge in the modelling of two of the three cases (1A and 1B) due to the presence of breaking waves at the offshore boundary. However, despite these difficulties, the energy dissipation rate inside the surf zone and the second breakpoint located at the inner breaker bar ($x=25$ m) are well captured by the numerical model.

The cross-shore variation of the lf- ($f<0.5f_p$ Hz) significant wave height, H_{slf}, is also shown in Fig. 7(a)–(c). In Tests 1A and 1B, the lf-wave transformation across the nearshore is well captured by the model. However, the numerical model overpredicts (underpredicts) the lf- energy inside the surf zone in case 1A (1B), which may be related with the uncertainties while forcing the numerical model assuming non-breaking waves at the generating boundary and owing to further difficulties in the physical experiment not accounted for in the numerical model. However, despite this problem the overall H_{slf} cross-shore structure is satisfactorily captured. On the other hand, the

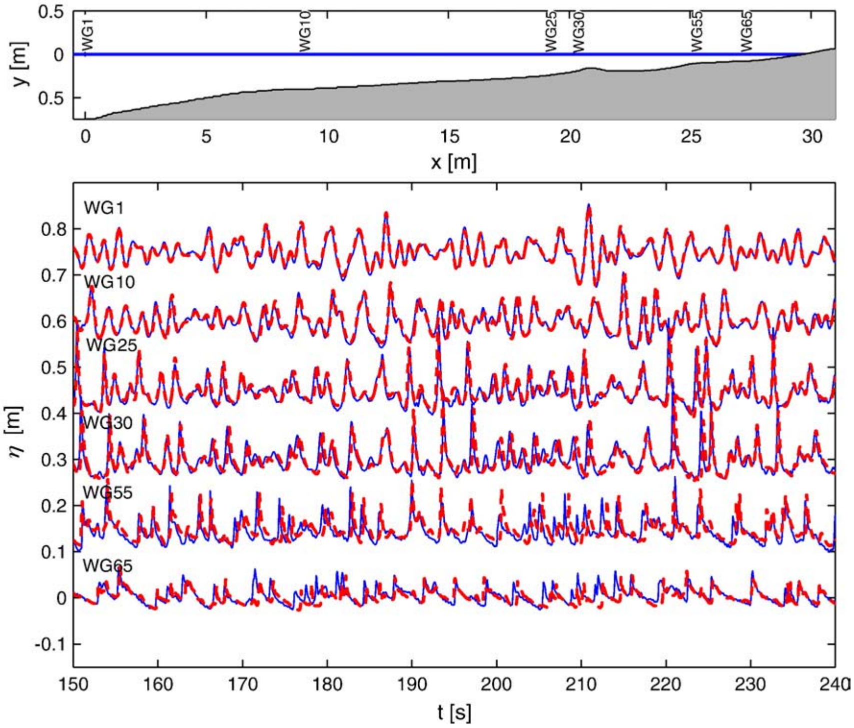

Fig. 4. Free-surface elevation time series at different cross-shore positions in Test 1C (solid line: observations; dashed line: model prediction).

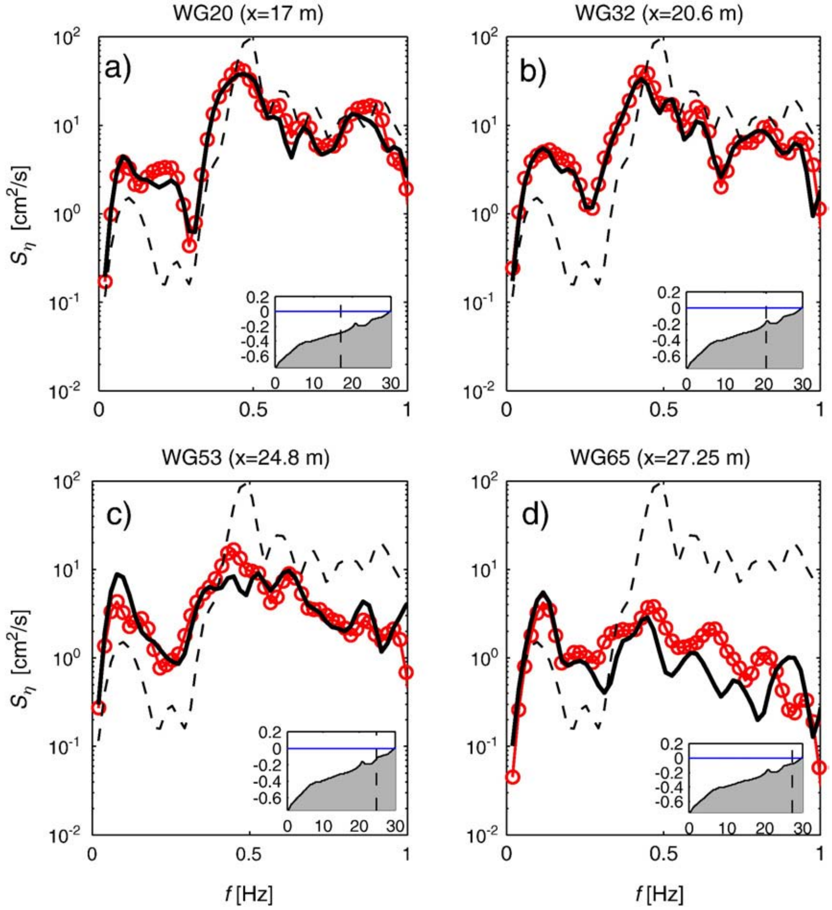

Fig. 5. Free-surface spectral density at (a) shoaling, (b) outer breaker bar, (c) inner breaker bar, and (d) inner surf zone (open circles: observations; dashed line: observed at $x=0$ m; solid line: model prediction) in Test 1A.

aforementioned uncertainties are not present during the forcing of Test 1C, where the agreement with observations inside the surf zone is remarkable. The model capability to capture the H_{slf} cross-shore variation in Test 1C motivated a more detailed study of lf-wave transformations in Section 5.

4.2. Higher-order moments

A key parameter for cross-shore sediment transport under near-breaking and breaking waves is the shape of the wave (Hsu and Hanes, 2004), which can be evaluated by means of higher order moments such as wave skewness and wave asymmetry (Elgar and Guza, 1985). The skewness and asymmetry are statistical measurements that indicate the horizontal (peaked) and vertical (pitched-forward) asymmetry of the wave form, respectively. Therefore, they are a criterion of nonlinearity which is expected to increase for breaking waves.

Fig. 9(a) shows the observed and predicted skewness across the flume in Test 1C for the low- and high- frequency band. The relatively small values of short-wave skewness increase to reach a local maximum around the outer breaker bar ($x=21$ m) with a subsequent monotonic onshore decrease reaching the minimum value close to shore. On the other hand, the low-frequency skewness is negative outside the surf zone but increases in the inner surf zone to reach a maximum value close to shore. The numerical model is able to reproduce all these features.

The short-wave asymmetry (Fig. 9b) begins with a small value close to zero at the seaward boundary, which is the expected value for nearly sinusoidal waves. The (negative) hf-asymmetry increases toward shore consistent with field observations (e.g. Raubenheimer, 2002). The model reproduces the observations with some differences near the inner breaker bar. The lf-wave asymmetry outside the surf zone seems to be controlled by the standing long-wave generated across the flume, alternating from positive to negative values and vice versa. Nevertheless, the long-wave asymmetry increases inside the surf zone, reaches a local maximum at the inner breaker bar and then decreases to negative values in the outer swash zone. In Tests 1A and 1B (not shown) discrepancies between observations and model predictions become significant, which may be ascribed to the fact that the numerical model is driven assuming non-breaking waves at the offshore boundary which does not happen in reality.

5. Low-frequency wave transformation: model–data comparison

Although most of the theoretical work regarding long-wave generation was developed some time ago (e.g. Longuet-Higgins and Stewart, 1960, 1962; Symonds et al., 1982; Schaffer, 1993), laboratory experiments focusing on the study of long-wave generation mechanisms had been limited, until very recently, to those of Kostense (1984). In the past few years, a thorough experimental verification of lf-wave transformations has been carried out (e.g. Janssen et al., 2003; Battjes et al., 2004; Baldock, 2006; van Dongeren et al., 2007; Grasso et al., 2007), based on high-spatial resolution laboratory measurements combined with highly controlled random wave conditions.

This section is devoted to the study of the model capability to accurately reproduce the physics behind the lf-wave transformation mechanisms reported in previous investigations. We adopt earlier data analysis methods (e.g. Janssen et al., 2003; Battjes et al., 2004; Thomson et al., 2006; van Dongeren et al., 2007) in order to be able to compare our computed results against the physical experiment observations. The numerical study is mainly focused on Test 1C in Boers (1996), since it is

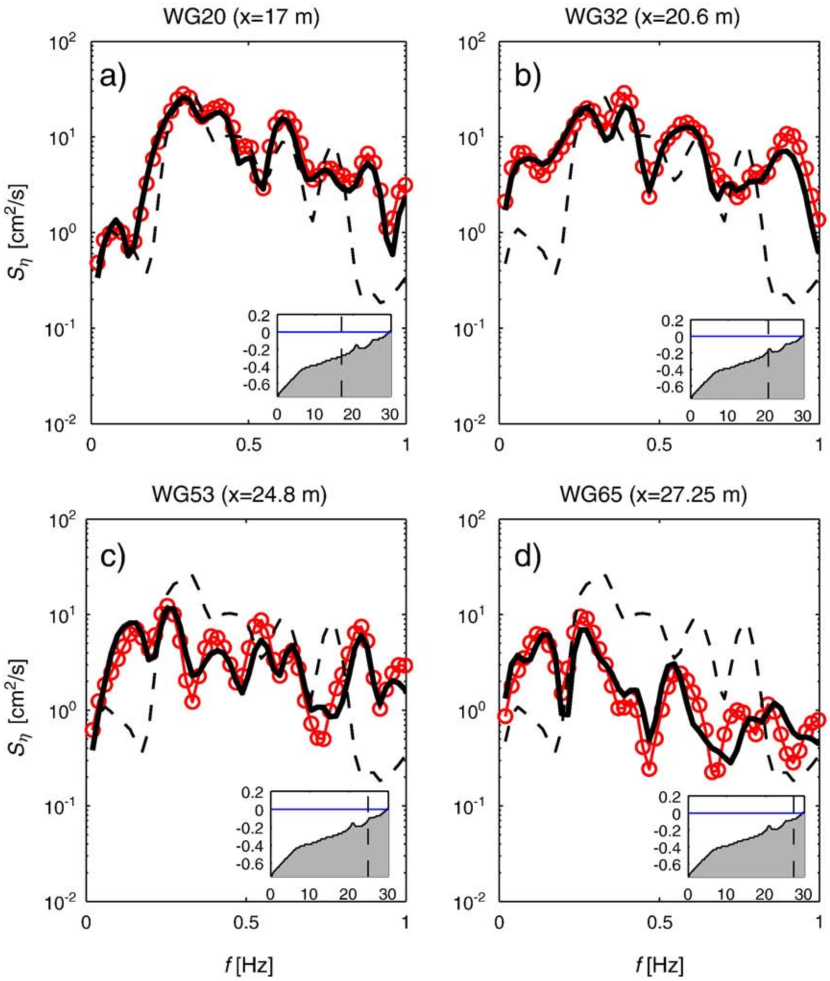

Fig. 6. Free-surface spectral density at (a) shoaling, (b) outer breaker bar, (c) inner breaker bar, and (d) inner surf zone (open circles: observations; dashed line: observed at $x = 0$ m; solid line: model prediction) in Test 1C.

the only suitable test for the study of the lf-wave transformation according to a previous study (Battjes et al., 2004).

5.1. Energy transfer

The so-called cross-correlation analysis between the short-wave envelope and the lf-wave is a commonly applied technique to determine their relationship. This technique was first applied to the identification of infragravity motions in the field by Tucker (1950), and since then it has been widely employed using field, laboratory, and numerical data. The lf-wave component is directly obtained from the low-pass filtered surface elevation (pressure) time series, and the short-wave envelope can be computed by means of the Hilbert transform operator of the surface elevation data, which is given by (Janssen et al., 2003),

$$A(x_p,t) = \left|\eta^{\text{high}} + \mathcal{H}\left\{\eta^{\text{high}}\right\}\right|^{\text{low}} \tag{5}$$

where η^{high} is the high frequency wave component (e.g. $0.5f_p < f$ Hz), $\mathcal{H}$ denotes the Hilbert transform operator, and $||^{\text{low}}$ represents the low-pass filtered ($f < 0.5f_p$) modulus where f_p is the peak frequency.

The normalized cross-correlation signal between two time series, $x(t)$ and $y(t)$, is estimated by (Bendat and Piersol, 1986)

$$R_{xy}(\tau) = \frac{\langle x(t)y(t+\tau)\rangle}{\sigma_x\sigma_y} \tag{6}$$

where τ is the time lag between the two signals (x and y), and σ_x and σ_y correspond to the standard deviation of each time series. The time series in this case are given by the low-pass-filtered surface elevation and the short-wave envelope squared obtained by Eq. (5) at every cross-shore location.

The cross-correlation analysis has been performed using measured and predicted free-surface elevation time series. This provides a means for performing a time-domain analysis of the relationship between the short-wave envelope and the long-wave propagation patterns across the nearshore. The values of the cross-correlation functions are plotted in the (τ–x)-plane as previously done in Janssen et al. (2003) using the same data set. The visual patterns of positive (ridges) and negative (troughs) correlation are used to analyze the short-wave envelope and long-wave transformations in the nearshore.

The cross-correlation between the lf-waves and the squared short-wave envelope, at every cross-shore position, for laboratory and numerical results are shown in Fig. 10(a) and (b), respectively. A trough of negative correlation at near-zero time-lag is observed from $x = 0$ m to $x = 21$ m in both figures. This is in agreement with the radiation stress theory (Longuet-Higgins and Stewart, 1962), which states that a maximum in the short-wave envelope corresponds to a depression (minimum) in the water level. A detailed comparison between observations and predictions (at different cross-shore positions) is presented in Fig. 10(c)–(e). In the shoaling region (Fig. 10c), the minimum correlation value is located at near zero time lag (negative trough in contourplot). However, as the shore is

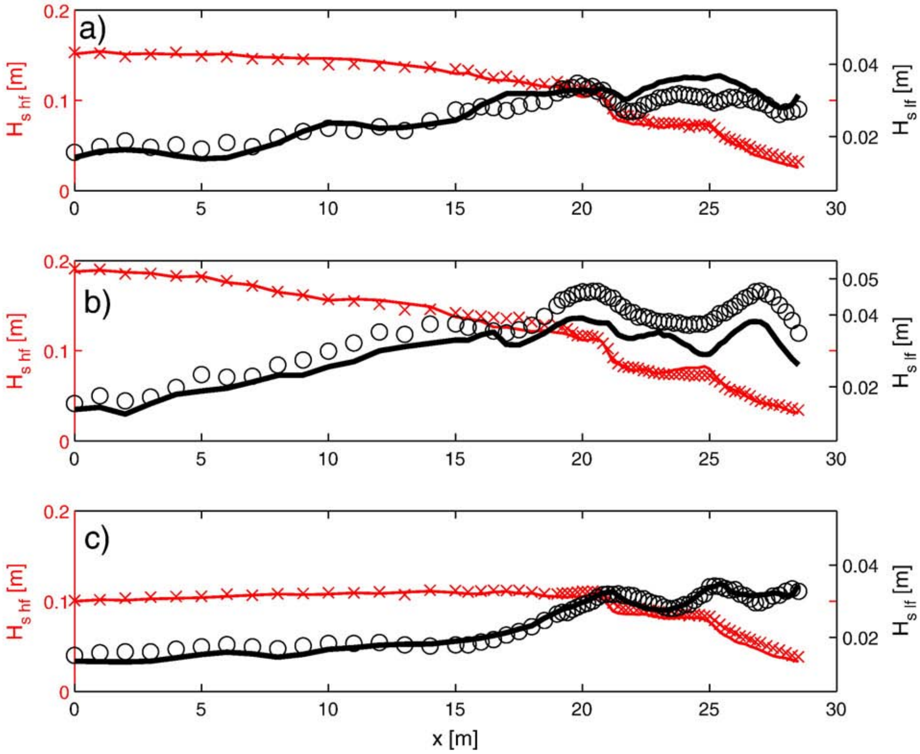

Fig. 7. High-frequency (crosses: ensemble averaged observations; thin solid line: model prediction) and low-frequency (open circles: ensemble averaged observations; thick solid line: model prediction) significant wave height as a function of cross-shore position in (a) Test 1A, (b) Test 1B, and (c) Test 1C.

approached, the long-waves lag behind the short-wave envelope, falling apart from the equilibrium value of $\tau = 0$ (Fig. 10d). This implies that the required mechanism (phase lag) for the energy transfer from hf- to lf-waves that takes place during short-wave shoaling is also predicted by the model. Finally, inside the inner surf zone, this correlation at near zero phase lag is reversed (see Fig. 10e) where the short-waves travel over the lf-waves (positive correlation) consistent with (Veeramony and Svendsen, 2001) laboratory observations. The agreement between the model and the observations is also satisfactory for the auto-correlation of the short-wave envelope and the low-frequency waves (not shown).

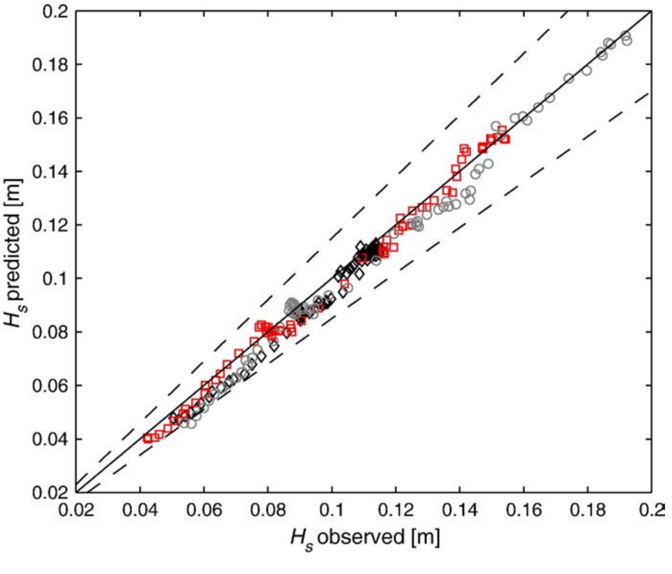

Fig. 8. Observed versus predicted total significant wave height (squares: Test 1A; circles: Test 1B; diamonds: Test 1C). Solid line: perfect agreement; dashed line: ±15% error bounds.

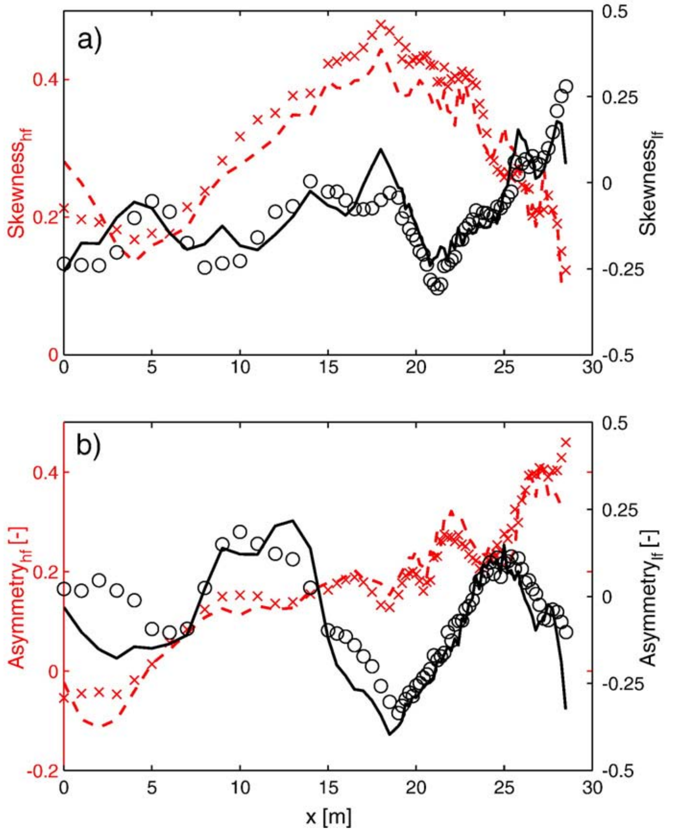

Fig. 9. High-frequency (crosses: ensemble averaged observations; dashed line: model prediction) and low-frequency (open circles: ensemble averaged observations; solid line: model prediction) wave (a) skewness and (b) asymmetry for Test 1C.

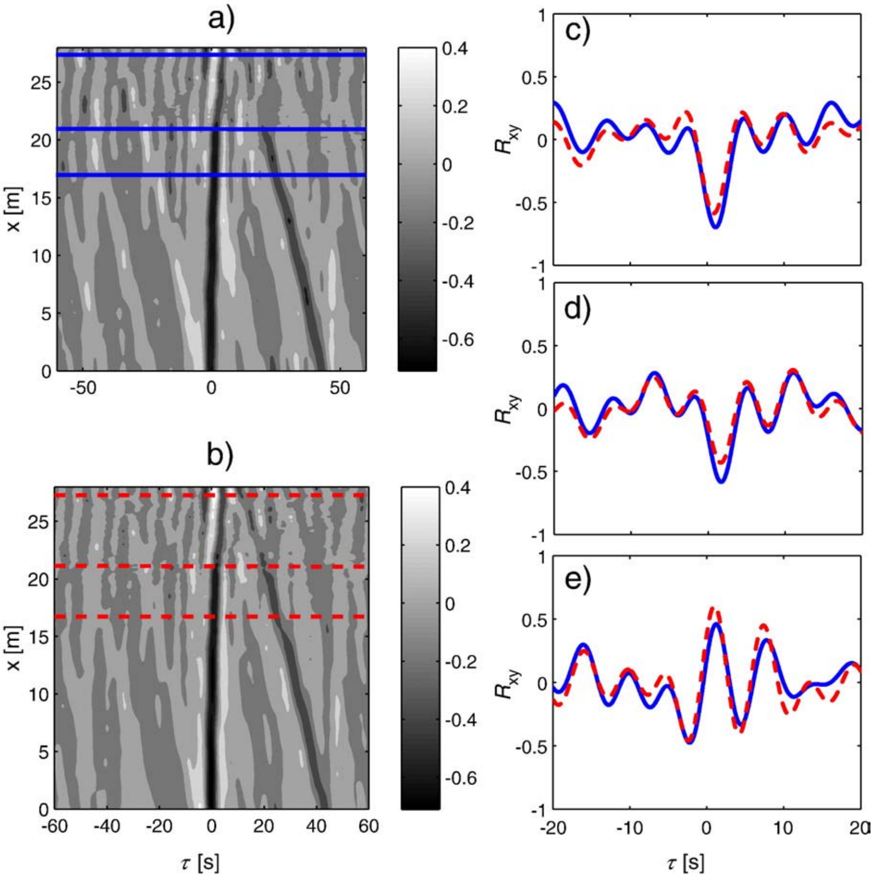

Fig. 10. Cross-correlation functions between squared short-wave envelope and low frequency motion at same cross-shore position using (a) observations and (b) model predictions. Model-data comparison (solid line: observed; dashed line: predicted) at (c) shoaling ($x = 17$ m), (d) breaking point ($x = 21$ m), and (e) inner surf zone ($x = 27.25$ m).

In addition, the comparisons between model predictions and observed time lags are shown in Fig. 11. The time-lags, obtained from the local minimum of the cross-correlation values at every cross-shore position, present values close to zero near the boundary. Small differences between observations and model predictions rely on the fact that the numerical model was forced assuming Longuet-Higgins and Stewart (1962) equilibrium solution at $x = 0$ m for this simulation. The negative time lags for $x < 8$ m in Fig. 11 were attributed by Janssen et al. (2003) to the presence of spurious free waves generated at the paddle and (or) to re-reflection. However, these negative lags are also present in the numerical model results where those effects are mostly suppressed. A closer analysis of these wiggles shows a strong correlation with the stationary lf-wave component (not shown) which may contribute to the negative values offshore. The numerical model reproduces the increasing phase lag during shoaling ($x = 8$ to 21 m), and most of the values inside the surf zone (where the lf-wave is already released). Some prediction points do not match the observations inside the surf region ($x > 21$ m) due to the insufficient grid resolution inside the surf zone (i.e. it was observed that the cross-correlation analysis is quite sensitive to grid resolution).

According to van Dongeren (1997) and Battjes et al. (2004), the energy transfer is only possible when an additional phase lag exists, which was shown to be well quantified by the numerical model (Fig. 11). However, it is also important to evaluate if the model is able to quantify the energy transfer from hf- to lf-waves taking place during wave shoaling (Battjes et al., 2004). Thus, the analysis of incident and reflected lf-wave components is performed. This decomposition is carried out in the frequency domain using the array method and the number of sensors proposed by Battjes et al. (2004) for the same data set. The model estimations for the incident and outgoing significant (lf-)

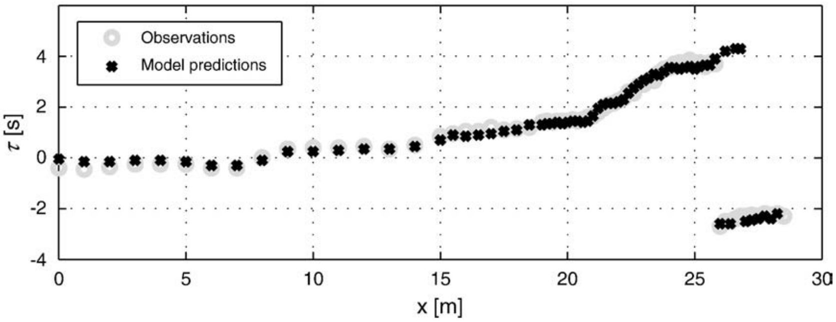

Fig. 11. Observed and predicted time lags.

wave heights (Fig. 12) are in agreement with the observations at all cross-shore positions, including within the surf zone ($x > 20$ m). The shoaling rate also exceeds Green's law ($\propto h^{-14}$) in the numerical model, meaning that the energy transfer from hf- to lf-waves is taking place. The relative mean error with respect to observations is of 5.55% and 4.45% with correlation r^2 of 0.98 and 0.97 for the incident and reflected wave components, respectively. These results show the COBRAS-UC capability for modelling the energy transfer to lower frequencies during wave shoaling, deshoaling, and breaking.

From the previously described decomposition analysis, it is possible to determine the shoaling rates of the incident long-wave components. The incident long-wave amplitude is evaluated by fitting a depth-dependent function (in the shoaling zone) of the form (e.g. van Dongeren et al., 2007)

$$\zeta^{(i)} \approx A h^{-\alpha} \tag{7}$$

where A is a constant of proportionality, and $-\alpha$ is an unknown power that is expected to lie between Green's law ($-1/4$) and the Longuet-Higgins and Stewart (1962) equilibrium solution ($-5/2$). Comparisons between model predictions and laboratory observations confirmed the model's capability (not shown) to satisfactorily predict the lf-wave shoaling rates α. The differences between observations and model predictions of α may be related to the fact that the model fails to predict the position of the release of the lf-waves due to the earlier breaking in the numerical model. In other words, the energy transfer from hf- to lf-waves is interrupted earlier in the model, decreasing the α values which are highly dependent on the breaking point location. This is consistent with the fact that deviations between observations and model predictions of α are more significant for higher frequencies (not shown).

In order to further study the model capability to predict the energy balance across the nearshore, the cross-shore gradients of energy flux are calculated based on the model results. This gradient represents the balance between the nonlinear interactions, dissipation effects, and wave reflection. The energy flux gradient at each point located between adjacent cross-shore positions is estimated based on (Herbers et al., 2000),

$$F_x = \frac{E_{n+1}(c_g)_{n+1} - E_n(c_g)_n}{x_{n+1} - x_n} \tag{8}$$

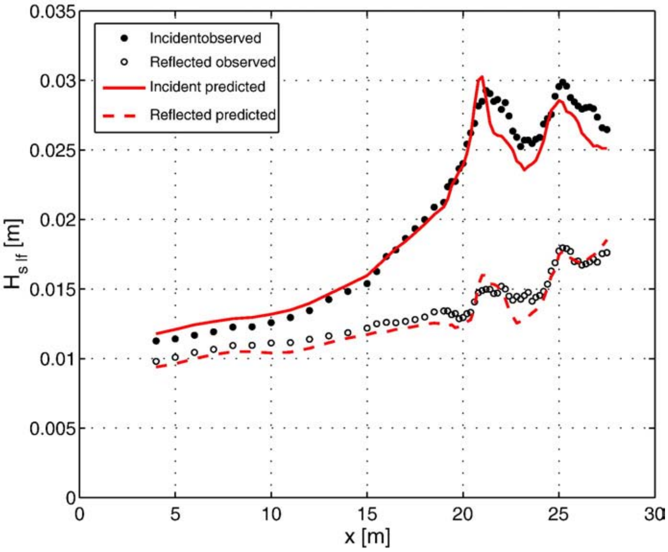

Fig. 12. Cross-shore variation of the incident and reflected H_{slf} (solid/open dots: incident/reflected laboratory wave height observations; solid/dashed line: incident/reflected model predictions Test B) for the total low-frequency band.

where $E_n(f)$ are the corresponding energy density spectra at every cross-shore position x_n, and the group velocity, c_g, in Eq. (8) is computed based on the local water depth and the peak frequency, f_p, in the incident wave spectrum. The model estimation of the energy flux gradient as a function of cross-shore position and frequency are shown in Fig. 13. The light (dark) patterns correspond to local energy gains (losses) at discrete frequencies with respect to an adjacent offshore location. The most relevant feature in this plot is the intermittence between positive and negative gradients at the primary spectral peak frequency (≈ 0.3 Hz). This pattern extends up to very close to shore. The nonlinear transfer to higher frequencies seems to dramatically increase shoreward of the first breakers ($f > 0.3$ Hz and $x < 17$ m in Fig. 13). The energy flux gradient at different cross-shore positions are compared against laboratory observations (Fig. 13a–d). During shoaling, there is a continuous energy exchange between the principal component ($f_p \approx 0.30$ Hz) and the higher and lower harmonics in order to conserve energy. The negative value near the spectral peak is balanced by positive values at higher and lower frequencies in Fig. 13 (a). However, the energy flux gradient is reversed in a short cross-shore distance (only one meter) where there is a positive value in the principal component and negative values for higher harmonics. Furthermore, the lf-energy band seems to keep growing at the expense of the energy from higher frequencies. At the outer breaker bar, there is a negative maximum in the energy flux gradient at the principal component and higher frequencies (Fig. 13c) owing to short-wave breaking. Differences between observations and predictions at higher frequencies may be related with insufficient grid resolution. The energy flux gradient prediction at low frequencies ($f < 0.20$ Hz) is very satisfactory considering that nonlinear interactions, dissipation, and partial reflection significantly contribute to its values.

5.2. Energy attenuation

Previous studies have pointed out the difficulties to simulate the low-frequency motions inside the surf zone (Janssen, 2006; Zijlema and Stelling, 2008). These motions are highly dependent on the accurate wave forcing, the energy transfer between triad of frequencies, the low-frequency dissipation, and the shoreline reflection (Herbers et al., 2000).

The numerical results show that the model is able to predict the cross-shore variation of the reflection coefficient in the shoaling zone and inside the surf zone (not shown). The latter is useful for the analysis of long-wave shoreline dissipation. According to Battjes et al. (2004), the significant difference between the incident and reflected long-wave amplitude observed at the shorewardmost sensor location for which the separated lf-wave height is available in Test 1C, implies a lf-energy loss of approximately 60% at locations shoreward of $x = 28$ m (see Fig. 10). In order to study this fact in more detail, the shoreline reflection coefficient is obtained as the ratio between the incident and reflected wave height. The shoreline reflection coefficient can be plotted as a function of β_H defined by (van Dongeren et al., 2007),

$$\beta_H = \frac{h_x}{\omega}\sqrt{\frac{g}{H}} \tag{9}$$

where H is the incident lf wave height at sensor WG66.

Very good agreement between observations (Fig. 14a) and model predictions (Fig. 14b) of the frequency dependent lf-dissipation is observed. Both observations and model predictions show, as expected, an increasing trend in energy dissipation for the higher low-frequencies.

Although Fig. 13 provides useful information about how the energy is distributed along the different frequencies, the interpretation of the cross-shore gradient in the lf-band is obscured by the significant amount of reflection occurring for these frequencies. Thus, in order to overcome

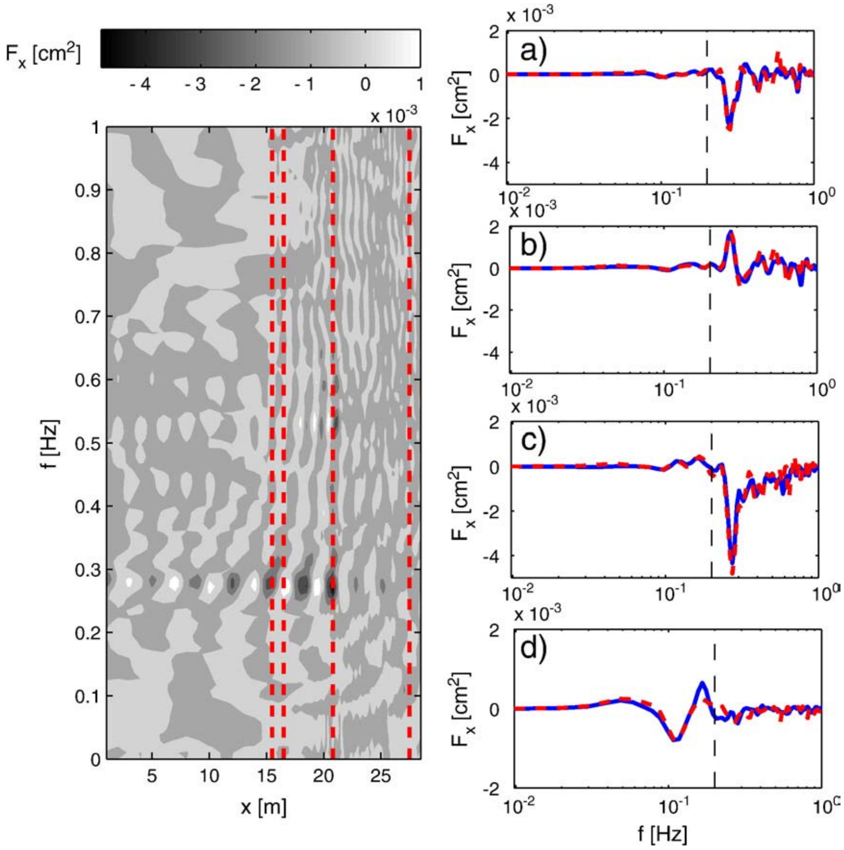

Fig. 13. Energy flux gradient as a function of cross-shore position and frequency (left). Model-data comparison (solid line: observed; dashed line: predicted) at (a)–(b) shoaling ($x = 16$ m and $x = 17$ m), (c) breaking point ($x = 21$ m), and (d) inner surf zone ($x = 27.25$ m). The vertical dashed line in (a)–(d) denotes the low-frequency limit at $f = 0.2$ Hz.

this limitation, the shoreward F^+ and seaward F^- energy fluxes, integrated over the lf-energy band ($0 < f < 0.2$ Hz), are computed (e.g. Thomson et al., 2006; Henderson et al., 2006) using the H_{slf} decomposition values from Fig. 12. Consistent with the wave height results, the energy flux value suggests a significant energy loss inside the surf zone for both observations and predictions (Fig. 15a). The model prediction reaches the maximum F^+ more seaward than the observations, which is consistent with the earlier breaking in the model. The cross-shore gradient of the shoreward (total) lf-energy flux is computed from adjacent sensors using Eq. (8) (Fig. 15b), where a nonzero value represents an

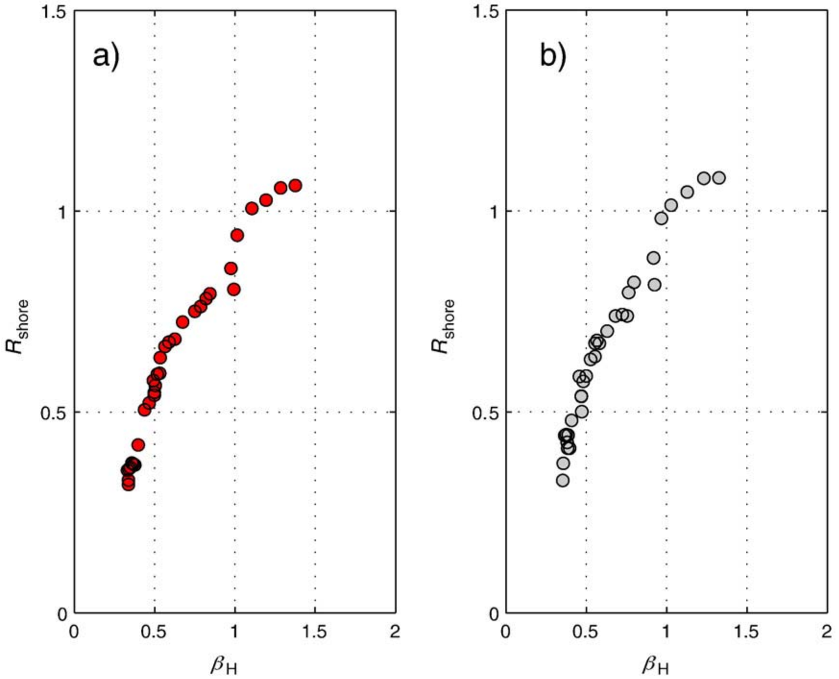

Fig. 14. Shoreline reflection coefficient, R, as a function of β_H computed from (a) the laboratory data and (b) numerical model.

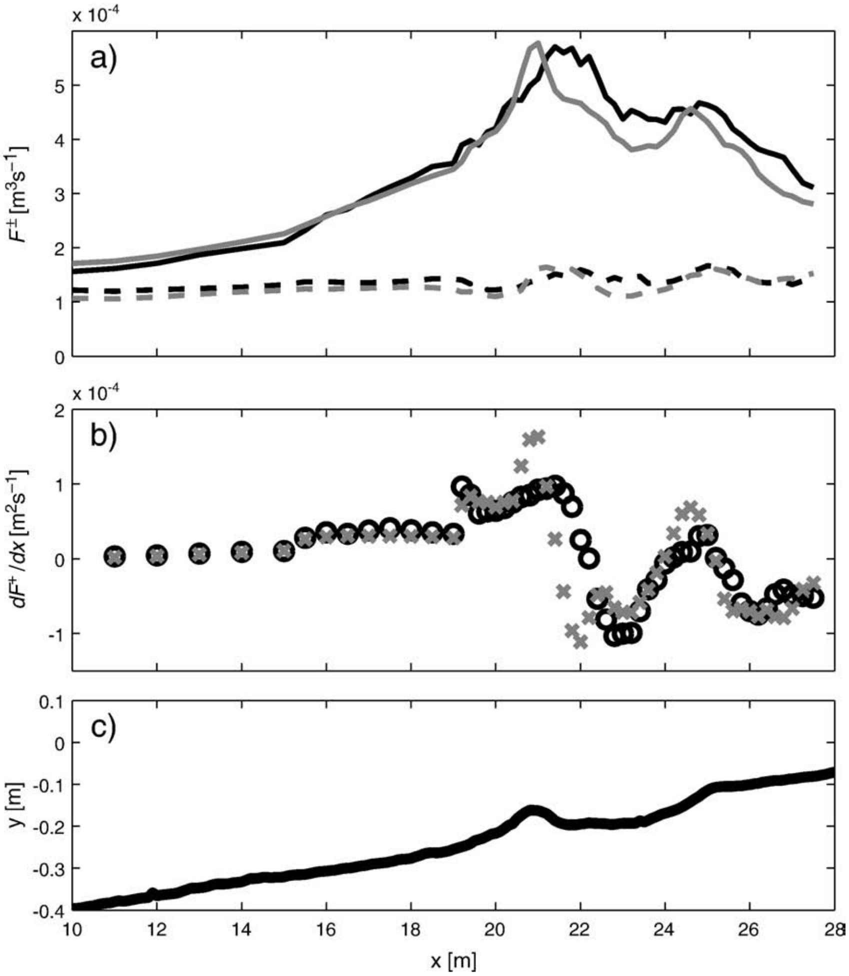

Fig. 15. (a) Energy flux integrated over the lf-energy band (solid line: incident; dashed line: reflected), (b) shoreward lf energy flux gradient, and (c) beach profile. Observations (dark) and model predictions (light).

energy flux gain (positive) or loss (negative) (Thomson et al., 2006). The gradient of F^+ shows a net gain at the expense of higher frequencies in the shoaling zone (see Fig. 13). At $x = 21$ m, there is a net loss of $\mathrm{d}F^+/\mathrm{d}x$ ascribed to the lf-energy transfer mechanism to higher frequencies during short-wave breaking according to Thomson et al. (2006). In the trough region, the short-wave is restored, decreasing the $\mathrm{d}F^+/\mathrm{d}x$ loss, and shoaling occurs again close to the inner-breaker bar. This allows a second net gain in F^+ extending to the inner-breaker bar crest where breaking occurs again followed by an energy flux loss. All these transformations are satisfactorily predicted by the numerical model.

6. Conclusions

We demonstrate the capability of a numerical model called COBRAS-UC, based on the RANS equations, for the study of nearshore hydrodynamics on a mild-slope beach. Surf zone hydrodynamics on a laboratory barred-beach, subject to different random wave conditions, is quantitatively simulated by the numerical model thanks to the implementation of a new boundary condition. Agreement between observations and model predictions is shown for the wave energy transformation, cross-shore (hf- and lf-) wave height variation, and free-surface elevation higher order statistics (skewness and asymmetry). Numerical results revealed an improvement in the modelling of low-frequency transformations inside the surf zone as compared with those reported from previous works. Lf-wave shoaling, the phase-lag between short- and lf-waves, the nearshore lf-wave energy balance, and the lf-wave dissipation are shown to be well quantified by the numerical model for one simulated test. This suggests that the model is suitable for studying physical process inside the surf zone in 1DH and 2DV.

During wave shoaling, the overall growth rate of the bound lf-waves is well predicted by the numerical model implying that the energy transfer from hf-waves to lf-waves during shoaling is well addressed by the model. This energy transfer is closely related to the phase-lag between the short-wave envelope and the bound wave observed in the laboratory/field during short-wave shoaling. This latter mechanism is also captured by the model. Inside the surf zone, the study of lf-wave dissipation is addressed by means of the shoreline reflection coefficients, and the energy flux gradient. The strong frequency dependence of lf-wave dissipation is in agreement with observations. The (incident) energy flux gradient analysis demonstrated that significant lf-energy losses occur during the short-wave breaking. This seems to be due to nonlinear-triad between lf- and hf-waves which drain the energy to higher frequencies for dissipation by short-wave breaking. It is also demonstrated, by means of numerical simulations, that the dissipation rate is highly dependent on the inner surf zone topography. The model capability to predict the lf-energy in this region implies that the wave forcing, energy transfer, energy dissipation, and shoreline reflection are well captured by the model.

The major drawbacks in the numerical model (COBRAS-UC) are related with the computational effort required and being restricted to 2DV flows. However, the quantitatively good results confirm that the model is suitable for the study of complicated surf zone processes and more important to improve the current parameterization of wave dissipation inside the surf zone.

Acknowledgments

The authors gratefully acknowledge Dr. Marien Boers for providing his valuable data. The work is funded by the project "Numerical and experimental modelling of hydrodynamic associated processes in the surf zone" (CTM2008-06044/MAR) from the Ministerio de Ciencia e Innovacion (Spain). ATF also acknowledges the financial support provided by the Mexican National Council of Science and Technology (CONACyT) for his graduate studies under the scholarship number 168776. J.L. Lara is indebted to the M.E.C. for the funding provided in the "Ramon y Cajal" Program. T. T. Janssen is greatly acknowledged for his comments and suggestions to improve the manuscript.

Appendix A. Wave generation

Longuet-Higgins and Stewart (1960) considered the non-linear interaction between two progressive wave trains and presented an explicit second-order solution for the surface elevation η and the velocity potential Φ:

$$\eta = \zeta_1^{(1)} + \zeta_2^{(1)} + \zeta_{12}^{(2)} \tag{A.1}$$

$$\Phi = \phi_1^{(1)} + \phi_2^{(1)} + \phi_{12}^{(2)} \tag{A.2}$$

where (ζ_1, ζ_2) and (ϕ_1, ϕ_2) are the first order solution expressed in terms of the wave amplitude a, the wave number k, the wave frequency σ, the phase angle ψ, and the water depth h. The single subscript denotes individual wave components, and the double subscripts refer to the corresponding bound wave component resulting from the quadratic interaction between frequency pairs. For simplicity, we only consider the difference interaction such as,

$$\zeta_{12}^{(2)} = \frac{a_1 a_2}{2g} \mathcal{D}_1 cos(\psi_1 - \psi_2) \tag{A.3}$$

and

$$\phi_{12}^{(2)} = \frac{\mathcal{D}_2 cosh((k_1 - k_2)(z + h)) sin(\psi_1 - \psi_2)}{g(k_1 + k_2) sinh(h(k_1 - k_2)) - (\sigma_1 + \sigma_2)^2 cosh(h(k_1 + k_2))} \tag{A.4}$$

where the $(\psi_1 - \psi_2)$ term correspond to the low-frequency interaction, and the difference interaction coefficients $\mathcal{D}_1$ and $\mathcal{D}_2$ are defined as (Longuet-Higgins and Stewart, 1960),

$$\mathcal{D}_1 = \frac{[2\sigma_1\sigma_2(\sigma_1 - \sigma_2)(1 + \alpha_1\alpha_2) + \sigma_1^3(\alpha_1^2 - 1) - \sigma_2^3(\alpha_2^2 - 1)]}{\sigma_1^2(\alpha_1^2 - 1) - 2\sigma_1\sigma_2(\alpha_1\alpha_2 - 1) + \sigma_2^2(\alpha_2^2 - 1)} \cdot \\ (\sigma_1 - \sigma_2)(\alpha_1\alpha_2 - 1) + (\sigma_1^2 + \sigma_2^2) - \sigma_1\sigma_2(\alpha_1\alpha_2 + 1) \tag{A.5}$$

and

$$\mathcal{D}_2 = -\frac{1}{2} a_1 a_2 [2\sigma_1\sigma_2(\sigma_1 - \sigma_2)(1 + \alpha_1\alpha_2) + \sigma_1^3(\alpha_1^2 - 1) - \sigma_2^3(\alpha_2^2 - 1)] \tag{A.6}$$

where $\alpha_1 = \coth(k_1 h)$ and $\alpha_2 = \coth(k_2 h)$.

For deriving the flux boundary condition in the numerical model, the measured wave signal is band-passed filtered and subsequently decomposed into Fourier components. Then, the second-order solution is sought as the sum of the primary components and the (difference) interactions between each pair, given as (Baldock et al., 1996),

$$\eta = \sum_{n=1}^{N} \zeta_n^{(1)} + \sum_{n=1}^{N} \sum_{m=n+1}^{N} \zeta_{nm}^{(2)} \tag{A.7}$$

$$\Phi = \sum_{n=1}^{N} \phi_n^{(1)} + \sum_{n=1}^{N} \sum_{m=n+1}^{N} \phi_{nm}^{(2)} \tag{A.8}$$

where $\zeta_n^{(1)}$ and $\phi_n^{(1)}$ are the first order solutions for the nth wave component, and $\zeta_{nm}^{(2)}$ and $\phi_{nm}^{(2)}$ are the second-order (difference) interactions between the nth and mth components. Finally, the second-order particle velocity is easily found from the velocity potential as $u^{(2)} = -\partial\Phi^{(2)}/\partial x$ and $w^{(2)} = -\partial\Phi^{(2)}/\partial z$.

References

Aagaard, T., Greenwood, B., 2008. Infragravity wave contribution to surf zone sediment transport – the role of advection. Mar. Geol. 251 (1–2), 1–14.

Baldock, T.E., 2006. Long wave generation by the shoaling and breaking of transient wave groups on a beach. Proc. R. Soc. A. 462, 1853–1876.

Baldock, T.E., Swan, C., Taylor, P.H., 1996. A laboratory study of non-linear surface waves on water. Philos. Trans. R. Soc. A 354, 649–676.

Battjes, J.A., Bakkenes, H.J., Janssen, T.T., van Dongeren, A.R., 2004. Shoaling of subharmonic gravity waves. J. Geophys. Res. 109 (C18).

Bayram, A., Larson, M., 2000. Wave transformation in the nearshore zone: comparison between a Boussinesq model and field data. Coast. Eng. 39, 149–171.

Bendat, J., Piersol, A., 1986. Random Data Analysis and Measurements. John Wiley, New York.

Boers, M., 1996. Simulation of a surf zone with a barred beach; Report 1: Wave heights and wave breaking. Tech. Rep. Rep.96-5, Comm. on Hydrol. and Geol. Eng., Dept. of Civ. Eng., Delft Univ. of Technol.

Boers, M., 2005. Surf zone turbulence. Ph.D. thesis, Delft Univ. of Technol.

Chen, Q., Kirby, J.T., Dalrymple, R.A., Shi, F., Thornton, E.B., 2003. Boussinesq modeling of longshore currents. J. Geophys. Res. 108 (C11).

Chopakatla, S.C., Lippmann, T.C., Richardson, J.E., 2008. Field verification of a computational fluid dynamics model for wave transformation and breaking in the surf zone. J. Waterw. Port Coast. Ocean Eng. 134, 71–80.

Chorin, A.J., 1968. Numerical solution of the Navier–Stokes equations. Math. Comput. 22, 745–762.

Chorin, A.J., 1969. On the convergence of discrete approximations of the Navier–Stokes equations. Math. Comput. 23, 341–353.

D'Alessandro, F., Tomasichio, G.R., 2008. The BCI criterion for the initiation of breaking process in Boussinesq-type equations wave models. Coast. Eng. 55, 1174–1184.

Elgar, S., Guza, R.T., 1985. Observations of bispectra of shoaling surface gravity waves. J. Fluid Mech. 161, 425–448.

Elgar, S., Guza, R.T., Raubenheimer, B., Herbers, T.H.C., Gallagher, E.L., 1997. Spectral evolution of shoaling and breaking waves on a barred beach. J. Geophys. Res. 102 (C7), 15,797–15,805.

Garcia, N., Lara, J.L., Losada, I.J., 2004. 2-D numerical analysis of near-field flow at low-crested breakwaters. Coast. Eng. 51, 991–1020.

Goda, Y., 1975. Irregular wave deformation in the surf zone. Coast. Eng. Jpn. 18, 313–326.

Grasso, F., Michallet, H., Barthélemy, E., 2007. Infragravity waves in mobile-bed laboratory experiments. Coast. Sediments 07, 235–247.

Guanche, R., Losada, I.J., Lara, J.L., 2009. Numerical analysis of wave loads for coastal structure stability. Coast. Eng. 56 (5–6), 543–558.

Henderson, S.M., Guza, R.T., Elgar, S., Bowen, A.J., 2006. Nonlinear generation and loss of infragravity wave energy. J. Geophys. Res. 111 (C12007).

Herbers, T.H.C., Russnogle, N.R., Elgar, S., 2000. Spectral energy balance of breaking waves within the surf zone. J. Phys. Oceanogr. 30, 2723–2737.

Hirt, C.W., Nichols, B.D., 1990. Volume of fluid (VOF) method for dynamics of free boundaries. J. Comput. Phys. 39, 201–225.

Hoefel, F., Elgar, S., 2003. Wave-induced sediment transport and sandbar migration. Science 299, 1885–1887.

Holman, R.A., Bowen, A.J., 1982. Bar, bumps and holes: models for the generation of complex beach topography. J. Geophys. Res. 87, 457–468.

Hsu, T.J., Hanes, D.M., 2004. Effects of wave shape on sheet flow sediment transport. J. Geophys. Res. 109 (C05025).

Hsu, T.-J., Liu, P.L.-F., 2004. Toward modeling turbulent suspension of sand in the nearshore. J. Geophys. Res. 109 (C06018).

Hsu, T.J., Sakakiyama, T., Liu, P.L.-F., 2002. A numerical model for wave motions and turbulence flows in front of a composite breakwater. Coast. Eng. 46, 25–50.

Janssen, T. T., 2006. Nonlinear surface waves over topography. Ph.D. thesis, Delft Univ. of Technol.

Janssen, T.T., Battjes, J.A., van Dongeren, A.R., 2003. Long waves induced by short-wave groups over a sloping bottom. J. Geophys. Res. 108 (C8).

Kaihatu, J.M., Kirby, J.T., 1995. Nonlinear transformation of waves in finite water depth. Phys. Fluids 7, 1903–1914.

Karunarathna, H., Chadwick, A., Lawrence, J., 2005. Numerical experiments of swash oscillations on steep and gentle beaches. Coast. Eng. 52, 457–511.

Kennedy, A.B., Chen, Q., Kirby, J.T., Dalrymple, R.A., 2000. Boussinesq modeling of wave transformation, breaking and run-up. i: 1d. J. Waterw. Port Coast. Ocean Eng. 126, 39–47.

Kirby, J.T., 2003. Boussinesq models and applications to nearshore wave propagation, surfzone processes and wave-induced currents. In: Lakhan, V.C. (Ed.), Advances in Coastal Modelling. Elsevier, pp. 1–41.

Kobayashi, N., Otta, A.W., Roy, I., 1987. Wave reflection and run-up on rough slopes. J. Waterw. Port Coast. Ocean Eng. 113 (3), 282–298.

Kobayashi, N., Wurjanto, A., 1992. Irregular wave setup and run-up on beaches. J. Waterw. Port Coast. Ocean Eng. 118, 368–386.

Kostense, J.K., 1984. Measurment of surf beat and set-down beneath wave groups. Proc. of the 19th International Conf. on Coastal Eng. ASCE.

Lara, J., Losada, I., Guanche, R., 2008. Wave interaction with low-mound breakwaters using a rans model. Ocean Eng. 35 (13), 1388–1400.

Lara, J.L., Garcia, N., Losada, I.J., 2006a. RANS modelling applied to random wave interaction with submerged permeable structures. Coast. Eng. 53, 395–417.

Lara, J.L., Losada, I.J., Liu, P.L.F., 2006b. Breaking waves over a mild gravel slope: experimental and numerical analysis. J. Geophys. Res. 111 (C11019).

Lin, P., Liu, P.L.-F., 1998a. A numerical study of breaking waves in the surf zone. J. Fluid Mech. 359, 239–264.

Lin, P., Liu, P.L.-F., 1998b. Turbulence transport, vorticity dynamics, and solute mixing under plunging waves in surf zones. J. Geophys. Res. 103 (15), 15,677–15,694.

Longuet-Higgins, M.S., Stewart, R., 1960. Change in the form of short gravity waves on long waves and tidal currents. J. Fluid Mech. 8, 565–583.

Longuet-Higgins, M.S., Stewart, R., 1962. Radiation stress and mass transport in gravity waves with application to surf beats. J. Fluid Mech. 13, 481–504.

Losada, I.J., Lara, J.L., Christensen, E.D., Garcia, N., 2005. Modelling of velocity and turbulence fields around and within low-crested rubble-mound breakwaters. Coast. Eng. 52, 887–913.

Losada, I.J., Lara, J.L., Guanche, R., González-Ondina, J.M., 2008. Numerical analysis of wave overtopping of high mound breakwaters. Coast. Eng. 55, 47–62.

Lynett, P.J., 2006a. Nearshore wave modelling with high-order Boussinesq-type equations. J. Waterw. Port Coast. Ocean Eng. 132 (5), 348–357.

Lynett, P.J., 2006b. Wave breaking velocity effect in depth-integrated models. Coast. Eng. 53, 325–333.

Lynett, P.J., Liu, P.L.-F., 2004. A two-layer approach to water wave modeling. Proc. R. Soc. Lond., A 460, 2637–2669.

Madsen, P.A., Sorensen, O.R., Schaffer, H.A., 1997. Surf zone dynamics simulated by a Boussinesq type model: I. model description and cross-shore motion of regular waves. Coast. Eng. 32, 255–287.

Mase, H., Kirby, J.T., 1992. Hybrid frequency-domain KdV equation for random wave transformation. Proc. of the 23 rd International Conf. on Coastal Eng. ASCE.

Munk, W.H., 1949. Surf beats. Eos Trans. 30, 849–854.

Péquignet, A.C.N., Becker, J.M., Merrifield, M.A., Aucan, J., 2009. Forcing of resonant modes on a fringing reef during tropical storm Man-Yi. Geophys. Res. Lett. 36 (L03607).

Puleo, J.A., Farhadzadeh, A., Kobayashi, N., 2007. Numerical simulation of swash zone fluid accelerations. J. Geophys. Res. 112.

Raubenheimer, B., 2002. Observations and predictions of fluid velocities in the surf and swash zones. J. Geophys. Res. 107.

Raubenheimer, B., Guza, R.T., 1996. Observations and predictions of run-up. J. Geophys. Res. 101 (C10), 25,575–25,587.

Raubenheimer, B., Guza, R.T., Elgar, S., 1996. Wave transformation across the inner surf zone. J. Geophys. Res. 101 (C10), 25,589–25,597.

Raubenheimer, B., Guza, R.T., Elgar, S., Kobayashi, N., 1995. Swash on a gently sloping beach. J. Geophys. Res. 100 (C5), 8751–8760.

Rodi, W., 1980. Turbulence Models and Their Application in Hydraulics -A-State-of-the-Art Review. Int. Assoc. for Hydryaul. Res, Delft, Netherlands.

Roelvink, J.A., Reniers, A., 1995. LIP 11D delta flume experiments. A dataset for profile model validation. Tech. Rep. Rep.H 2130, Delft Hydraulics.

Sand, S.E., 1982. Long waves in directional seas. Coast. Eng. 6, 195–208.

Schaffer, H.A., 1993. Infragravity waves induced by short-wave groups. J. Fluid Mech. 247, 551–588.

Schaffer, H.A., Madsen, P.A., Deeigard, R., 1993. A Boussinesq model for wave breaking in shallow water. Coast. Eng. 20, 185–202.

Symonds, G., Huntley, D.A., Bowen, A.J., 1982. Two dimensional surfbeat: long wave generation by a time-varying breakpoint. J. Geophys. Res. 87, 492–498.

Thomson, J., Elgar, S., Raubenheimer, B., Herbers, T.H.C., Guza, R.T., 2006. Tidal modulation of infragravity waves via nonlinear energy losses in the surfzone. Geophys. Res. Lett. 33 (L05601).

Torres-Freyermuth, A., Losada, I.J., Lara, J.L., 2007. Modeling of surf zone processes on a natural beach using Reynolds-Averaged Navier–Stokes equations. J. Geophys. Res. 112 (L05601).

Troch, P., Rouck, J.D., 1999. An active wave generating-absorbing boundary condition for VOF type numerical model. Coast. Eng. 38, 223–247.

Tucker, M.J., 1950. Surf beats: Sea waves of 1 to 5 min. period. Proc. R. Soc. London, Ser. A 202, 565–573.

van Dongeren, A., Battjes, J., Janssen, T., van Norloos, J., Steenhauer, K., Steenbergen, G., Reniers, A., 2007. Shoaling and shoreline dissipation of low-frequency waves. J. Geophys. Res. 112 (C02011).

van Dongeren, A. R., 1997. Numerical modeling of quasi-3D nearshore hydrodynamics. Tech. Rep. Res. Rep.CACR-97-04, Cent. for Appl. Coastal Res., Univ. of Delaware, Newark.

van Dongeren, A.R., Svendsen, I.A., 1997. Absorbing-generating boundary conditions for shallow water models. J. Waterw. Port Coast. Ocean Eng. 123 (6), 303–313.

Veeramony, J., Svendsen, I.A., 2000. The flow in surf-zone waves. Coast. Eng. 39, 93–122.

Veeramony, J., Svendsen, I.A., 2001. Wave breaking in wave groups. J. Waterw. Port Coast. Ocean Eng. 127, 200–212.

Watson, G., Peregrine, D.H., 1992. Low frequency waves in the surf zone. Proc. of the 23 rd International Conf. on Coastal Eng. ASCE.

Zijlema, M., Stelling, G., 2008. Efficient computation of surf zone waves using the nonlinear shallow water equations with non-hydrostatic pressure. Coast. Eng. 55 (10), 780–790.